Materials & Design 225 (2023) 111464

Contents lists available at ScienceDirect

Materials & Design

journal homepage: www.elsevier.com/locate/matdes

# 3D-printed magnesium-doped wollastonite/nano-hydroxyapatite bioceramic scaffolds with high strength and anti-tumor property

Huifeng Shao [a,b,c,d,1,*], Zhuoluo Jing [a,1], Pengcheng Xia [e,1], Tao Zhang [a], Zhiheng Nian [a], Wanshun Liu [e], Jiahua Zhu [a], Youping Gong [a], Rougang Zhou [a,f], Yong He [b,c,*], Qingqiang Yao [e,*]

[a] School of Mechanical Engineering, Hangzhou Dianzi University, Hangzhou 310018, China
[b] State Key Laboratory of Fluid Power and Mechatronic Systems, School of Mechanical Engineering, Zhejiang University, Hangzhou 310027, China
[c] Zhejiang Guanlin Machinery Limited Company, Anji 313300, China
[d] Jiangsu Key Laboratory of 3D Printing Equipment and Manufacturing, Nanjing Normal University, Nanjing 210000, China
[e] Department of Orthopaedic Surgery, Institute of Digital Medicine, Nanjing First Hospital, Nanjing Medical University, Nanjing 210006, China
[f] Wenzhou Institute of Hangzhou Dianzi University, Wenzhou 325024, China

## HIGHLIGHTS

- Customized magnesium-doped wollastonite/nano-hydroxyapatite bioceramic scaffolds with precise porous structures were fabricated by 3D printing and coating technique.
- Composite bioceramic scaffold with 15 μm coating thickness exhibited the highest mechanical properties.
- Nano-hydroxyapatite coating can effectively inhibite the proliferation of human osteosarcoma cells.
- Composite bioceramic scaffold had significantly enhanced osteogenic induction on Rat bone marrow stem cells.

## GRAPHICAL ABSTRACT

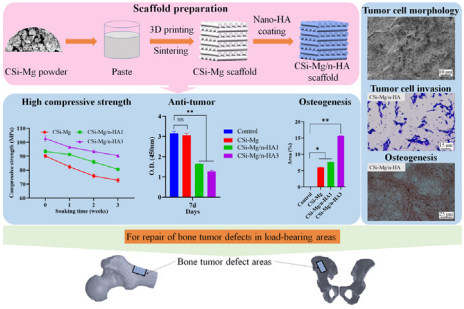


## ARTICLE INFO

*Article history:*
Received 14 October 2022
Revised 27 November 2022
Accepted 3 December 2022
Available online 6 December 2022

*Keywords:*
3D printing
Magnesium-doped wollastonite
Bioceramic scaffolds
Anti-tumor property
Nano-hydroxyapatite

## ABSTRACT

It is still a major challenge to remove tumor cells and fill bone defects after tumor resection. Combined with the 3D printing technology, the composite bioceramics scaffolds were fabricated with interconnected porous magnesium-doped wollastonite (CSi-Mg) scaffolds as the architecture and nano-hydroxyapatite (*n*-HA) as the surface. The influence of manufacturing process on the *n*-HA layer thickness and degradation performance, biological performance and anti-tumor performance of the composite scaffolds were investigated. The *n*-HA surface layer could effectively retard the degradation rate of CSi-Mg scaffolds and maintain high mechanical strength (over 90 MPa) after immersion in simulated body fluid for 3 weeks. Meanwhile, CSi-Mg/n-HA3 scaffold induced about 50 % of cell death for human osteosarcoma cells (MG-63) in vitro. CSi-Mg/*n*-HAx (x = 1, 3) scaffolds could improve the osteogenic performance of Rat BMSC. These findings demonstrate that the bioceramic composite scaffold with high strength, good osteogenic performance and anti-tumor performance is promising for the treatment of tissue injury after resection of osteosarcoma.



* Corresponding authors at: School of Mechanical Engineering, Hangzhou Dianzi University, Hangzhou 310018, China (H. Shao). State Key Laboratory of Fluid Power and Mechatronic Systems, School of Mechanical Engineering, Zhejiang University, Hangzhou 310027, China (Y. He). Department of Orthopaedic Surgery, Institute of Digital Medicine, Nanjing First Hospital, Nanjing Medical University, Nanjing 210006, China (Q. Yao).
*E-mail addresses:* shaohf@zju.edu.cn (H. Shao), yongqin@zju.edu.cn (Y. He), yaoqingqiang@126.com (Q. Yao).
[1] Co-first author.

https://doi.org/10.1016/j.matdes.2022.111464
0264-1275/

## 1. Introduction

Osteosarcoma is a common malignant tumor, mainly occurring in children and adolescents, The clinical presentation of osteosarcoma is not obvious, and there is no spontaneous fracture or severe pain in the early stage. As a result, the disease is not easy to diagnose, but tumors grow rapidly [1]. Osteosarcomas can cause large bone defects and limited movement, and can metastasise to the lungs [2]. At present, the treatment of osteosarcoma is mostly to remove the tumor site, and then supplemented by chemotherapy and other means [3]. However, excision usually results in a bone defect that exceeds the tissue's ability to heal itself [4], Moreover, it is difficult to completely eliminate tumor cells after resection and chemotherapy, and residual tumor cells may lead to local recurrence and surgical failure. Additionally, there is potential risk of bacterial infection during surgical procedure [5]. Based on this situation, a treatment method for bone defects after bone cancer surgery has been highly concerned and widely studied by researchers.

One of the most effective methods to treat bone defect is filling bone scaffold [6]. Bone regeneration is a complex process as molecular, biochemical, mechanical and cellular aspects have to be considered [7]. The ideal bone scaffold should not only have the appropriate mechanical properties, biological activity, degradability [8] and angiogenesis, but also have the function of killing tumor cells or inhibiting their growth. In the field of bone tissue repair, calcium silicate (CSi) bioceramics have attracted extensive attention due to their excellent bone conductivity, biological activity and degradability. The mechanical properties of calcium silicate ceramics can be effectively improved by doping magnesium into CSi during the synthesis process. Chemical co-precipitation method is a material manufacturing method that mixes different substances in solution, reacts to produce sediment, and forms the corresponding powder particles after drying the sediment. The material can be mixed evenly, and the chemical composition of the material is single. It has the advantages of simple process and good product performance, which is often used to prepare inorganic materials[9]. It has been pointed out that magnesium-doped wollastonite (CSi-Mg) bioceramic material has high mechanical properties and biological activity, and it has broad prospects for repairing bone defects [9–11]. In addition, additive manufacturing technology enables the creation of bone filled scaffolds with complex shapes, internal pores and controllable porosity [12–14]. The interconnected macropores are essential to supply sufficient space for cellular activity, nutrient transport and cell–cell interactions [15]. Extrusion 3D printing is an additive manufacturing method in which bioceramics inks made of organic binders and bioactive ceramics are stacked layer by layer to form a fixed 3D porous structure with interconnected pores. 3D-printed CSi-Mg scaffolds can promote the formation of new bone in the bone defects of rabbit mandible and skull [16–18]. The degradation of silicon and magnesium ions [17] is conducive to osteogenesis [19–21]. Although CSi-Mg scaffold has incomparable advantages compared with other bioactive materials, the slightly faster degradation rate, which mismatches with the bone tissue regeneration during the new bone ingrowth, restricts its application in the field of bone repair.

Hydroxyapatite (HA), which has the similar chemical composition as bone, is the most studied calcium phosphate ceramics [22]. HA has been shown to have good cell affinity and promote osteoblast adhesion and proliferation [23,24], but it has a low degradation rate [25]. In recent years, studies have also shown that nano-hydroxyapatite (*n*-HA) has anti-tumor effects [26–28]. And it can inhibit tumor growth, prevent tumor metastasis and improve survival rate of tumor-bearing rabbits [29]. These all reveal that the value of *n*-HA both as a bone-regenerating material and as an anti-tumor material. Therefore, we attempted to adsorb *n*-HA on the surface of CSi-Mg bioactive scaffolds to reduce degradation rate of CSi-Mg scaffolds and improve the mechanical properties, and the CSi-Mg/*n*-HA composite scaffolds with good anti-tumor property are also suitable for bone defects after bone cancer surgery.

In this study, the CSi-Mg powder was synthesized by chemical co-precipitation method and the CSi-Mg scaffold was fabricated by 3D printing technology, it was hypothesized that the *n*-HA surface layer can control the degradation rate of the CSi-Mg-based porous ceramics. The influence of manufacturing process parameters on the thickness of *n*-HA layer was studied, and the influence of the *n*-HA layer thickness on the degradation performance, mechanical properties and biological properties of the 3D printing CSi-Mg/*n*-HA composite scaffolds were analyzed, as well as the anti-tumor effect and osteogenesis performance of the composite scaffolds were explored.

## 2. Materials and methods

### 2.1. CSi-Mg and n-HA powders

The CSi-Mg powders with Mg doping (10 % Ca was substituted by Mg in CSi) were synthesized by a conventional chemical co-precipitation method as described in our previous work [9]. The as-calcined CSi-Mg powders were ground in a planetary ball miller (MP-2L; Chishun Sci&Tech Co., China) using 3.5 mm diameter zirconia ball media in ethanol for 6 h. The particle size distribution of the resulting CSi-Mg powders was below 10 μm. The *n*-HA powders were purchased from Shanghai Aladdin Bio-Chem Technology Co., ltd. The chemical composition of all materials was listed in the Supporting information, Table S1.

### 2.2. Preparation of CSi-Mg/n-HA composite scaffolds

For layer-by-layer printing of the CSi-Mg based scaffolds, the paste was prepared by mixing 5.8 g of powders with 4.0 g of 6 % polyvinyl alcohol (Sinopharm Chemical Reagent Co., ltd) solution. The paste was then added to a commercial syringe and extruded through a conical nozzle by the movement of a piston rod. A rectangular porous scaffold model with 3D architecture was designed using software. The moving speed of the dispensing unit was set to 6 mm/s, the nozzle diameter was 500 μm, the porosity was 55 %, and the layer thickness was 0.35 mm. Then, the scaffold samples were dried at 80℃ overnight to remove excess water in the pore struts, and followed by sintering in a micro-controller-controlled temperature furnace at a target temperature of 1140℃, in air atmosphere using similar heating schedules (heating rate was 2℃/min while maintaining at 320℃ and 500℃ for 45 and 60 min, respectively) and held at target temperature for 4 h, followed by cooling naturally (Table S2).

Sodium alginate (SA) (Sinopharm Chemical Reagent Co., ltd) solutions (1.0 %, 1.5 %, 2.0 % (w/v)) were prepared with distilled water, *n*-HA powders were added to sodium alginate solution and ethanol (Sinopharm Chemical Reagent Co., ltd), respectively, to obtain 4 % (w/w) *n*-HA/SA solution and *n*-HA/ethanol solutions (0.10 g/ml, 0.15 g/ml, and 0.20 g/ml). The CSi-Mg scaffolds were first dipped in *n*-HA/ethanol solution under vacuum for 2 min and stirred in air for target time (5 min, 10 min, or 15 min), followed by drying for 15 min. Next, the scaffolds were immersed in *n*-HA/SA solution under vacuum until no bubbles emerged from the scaffolds (10 min) followed by drying (70℃, 15 min). These scaffolds prepared in *n*-HA/ethanol solution and *n*-HA/SA solution

for 1, 2, 3 times were respectively named as CSi-Mg/n-HA1, CSi-Mg/n-HA2, CSi-Mg/n-HA3.

### 2.3. Physicochemical characterization of the powders and scaffolds

The phase composition of the CSi-Mg and *n*-HA powders was verified by X-ray diffractometer (XRD; Rigaku Co., Japan) at 40 kV/40 mA. Data were collected between 20° and 60° with a step of 0.02°/2θ and a dwell time of 1.5 s to identify any crystalline phase of the powders. The inorganic ion content in CSi-Mg powder was measured by inductively coupled plasma-optical emission spectrometry (ICP-OES; Thermo Icap 6000 series). The powders were observed by using the scanning electron microscopy (SEM, S-4800; Japan) at 10 kV. The particle size distribution was analyzed by dynamic light scattering (DLS, Malven Instrument 2000) in purified water medium.

### 2.4. Mechanical test of scaffolds

The compressive strength and elastic modulus of the bioceramic scaffolds (7 × 7 × 7 mm) were tested the direction parallel to the pore orientation (along the vertical Z direction) on a universal testing machine (Instron 5566, Germany) at a cross-head speed of 0.5 mm/min. Six samples were used for replicates of this experiment. The test was carried out by the procedure described in ASTM C773-88. The elastic modulus was determined from the linear region of the stress versus strain response.

### 2.5. Degradation and mechanical stability evaluation in vitro

In order to evaluate the weight loss (degradation) of the scaffolds (7 × 7 × 7 mm), the scaffolds (W0) were respectively immersed in simulated body fluid (SBF) with an initial pH 7.40 at 37℃ with a liquid/solid ratio of 200 mL/g. After immersing for every 48 h, the pH of solutions was measured. The samples were rinsed with ethanol and then dried up to mass constancy (Wt) before weighing. The weight decrease was expressed as the following equation: weight loss = Wt/ W0 × 100 %. The compressive strength of the as-dried scaffolds was also determined by Instron testing machine.

### 2.6. Assessment of bioactivity in SBF

The scaffolds were immersed in SBF at 37℃, the formation of HA and the degradation of SA were monitored on the surface of samples for different time stages. After soaking for 1 week to 4 weeks, the scaffolds were washed with ethanol and observed using SEM. Prior to examination, the samples were coated with a thin layer of gold.

### 2.7. Cell culture in vitro

MG63 cells were provided by Procell (China). The MG63 cells were cultivated in Dulbecco's modified Eagle medium high-glucose (DMEM) (KeyGEN BioTECH, China), which included 10 % fetal calf serum (Procell, China), 100 U/mL penicillin and 100 mg/mL streptomycin (Procell, China), at a 37℃ incubator with 5 % $CO_2$.

Rat bone-marrow stem cells (Rat BMSC) were provided by Procell (China). The Rat BMSC were cultivated in Dulbecco's modified Eagle medium low-glucose (DMEM) (KeyGEN BioTECH, China), which included 10 % fetal calf serum (Procell, China), 100 U/mL penicillin and 100 mg/mL streptomycin (Procell, China), at a 37℃ incubator with 5 % $CO_2$ [30].

The extracts of scaffolds were prepared in advance for research in vitro. The preparation process of the extracts was briefly described as follows: prepare the CSi-Mg, CSi-Mg/n-HA1, CSi-Mg/n-HA3 (diameter of 10 mm, thickness of 1 mm). Then these four scaffolds were soaked into 1 mL serum-free medium, and incubated on the shaker at 37 °C for 24 h respectively. The medium was then extracted and sterilized with a 0.22 μm Millipore filter.

#### 2.7.1. Apoptosis was detected by Annexin V-EGFP PI double staining

Monolayer adherent cells at logarithmic growth stage were digested with 0.25 % trypsin and blown into single cells. The cells were inoculated into 6-well plates at a density of $10 \times 10^4$ / dish and cultured in a 5 % $CO_2$ incubator at 37℃ [31]. After the cells were attached to the wall, they were divided into experimental groups for experimental treatment. After 7 days of culture, cells were collected, stained with Annexin V-EGFP Apoptosis Detecyion kit (KeyGEN BioTECH China) and detected by BECKMAN COULTER CytoFLEX flow cytometer.

#### 2.7.2. Cell viability staining

The cells were inoculated onto the scaffolds in an incubator of 37℃ and 5 % carbon dioxide. After 3 and 7 days of culture, the culture medium was sipped and washed with PBS for 3 times. According to the manufacturer's instructions, the living and dead cells were detected by calcein /PI cell viability/cytotoxicity assay kit (Beyotime, Cat: C2015M, Shanghai, China). The cells were then observed under a laser scanning confocal microscope (Olympus, Japan). Cell survival was calculated by mean fluorescence intensity.

#### 2.7.3. Caspase-3 colorimetric assay

Human bone cancer cell MG63 was divided into four groups (control, CSi-Mg, CSi-Mg/n-HA1, CSi-Mg/n-HA3). All the MG63 cells were digested by trypsin, then the digested cells were centrifuged (4℃, 2000 rpm, 5 min) and resuspended in 150 μL of a lysis buffer and 1.5 μL DTT from a caspase-3 (KGA202, KeyGEN, China), placed on ice for 1 h, and vortexed four times for 10 s each time. The cell suspension was centrifuged (10,000 rpm, 1 min), and the supernatant was transferred to a 1.5-mL centrifuge tube, which was then placed on ice. Approximately 50 μL of a 2 × reaction buffer and 5 μL of the caspase-3 substrate were added to each 50-μL sample, incubated at 37℃ in the dark for 4 h, and then analyzed by using a microplate reader at a wavelength of 405 nm [32].

#### 2.7.4. Wound-healing assay

In the cell scratch experiment, MG63 cells were cultured in 6-well plates (Corning, USA) and incubated until reaching 80 to 90 % confluence. The lines were gently crossed vertically with the head of a 200 ul spear to ensure that there were no cells at the lines. PBS was used for 3 times to wash away the lines. The serum-free medium extract containing each grouping material prepared in advance was added to the well plate. At 0 h and 24 h, cell scratch pictures were taken under microscope (Nikon, Japan), and the cell migration of each group was analyzed by Image J (Ver 1.53q) software.

#### 2.7.5. Colony formation assay

The cells were digested to make a suspension and counted; 1,000 cells were seeded in each well of a 6-well plate. The medium was changed every 3 days. After 10 days, the cells were fixed with 4 % paraformaldehyde for 15 min, then stained with crystal violet solution for 30 min and photographed with a digital camera, and the clone formation rate was calculated.

#### 2.7.6. Transwell migration asssy

In Transwell chamber (pore size 8 μm; Costar, NY, USA), $2 \times 10^4$ cells were cultured with 200 μL serum-free medium in the upper chamber, and 700 μL medium plate containing 10 % FBS in the lower chamber. The cells were cultured at 37 °C and 5 % $CO_2$ for 24 h. The cells were fixed with 500 μL 4 % paraformaldehyde at

room temperature for 20 min, then stained with 500 μL crystal violet solution for 30 min. The cells in the upper chamber were wiped and the chamber was cleaned with deionized water and then photographed with a microscope (Olympus, Japan).

*2.7.7. RNA extraction and qRT-PCR*

Total cellular RNA was extracted by TRIzol reagent and centrifugal column method (TransGen, China). RNA concentration and mass were measured by NanoDrop spectrophotometer (ND-100, Thermo Fisher Scientific). QRT-PCR was performed and the mRNA expression levels were normalized to GAPDH (Thermo Fisher Q5 ABIQuantStudio 5 U.S.). Each sample was determined three times. Relative gene expression was determined by 2^-ΔΔCT. The forward and reverse primer sequences utilized are listed in Table S3.

*2.7.8. Cell morphology staining*

100,000 cells were inoculated onto the scaffold and incubated for 24 h. The scaffold was transferred to a new culture plate. Part of the scaffold was removed on the third day and the seventh day of culture. 0.5 % TritonX-100 was permeated for 5 min, then atrin-tr Acker Green was incubated with the cells at room temperature for 30 min. Finally, cells were stained with DAPI. Laser scanning confocal microscope (Olympus, Japan) 4 × is used for photography.

*2.7.9. CCK-8 assay*

The cells were digested into single cell suspension and counted to $2 \times 10^4$/mL. 100 μL cells were spread in 96-well plates peer well. Each sample was set with 6 multiple holes, and 100 μL PBS was added into the edge holes. 10 μL CCK-8 (Shanghai yuanye Bio-Technology, China) was added to each well on the 1st, 3rd, 5th and 7th day, and incubated for 2 h. The OD value of CCK-8 was 450 nm by microplate reader (MOLECULAR DEVICES).

*2.7.10. Alizarin-red s assay*

Briefly, Rat BMSC were plated into a 24-well plate and cultured in osteogenic inductive media with different scaffolds extracts (CSi-Mg, CSi-Mg/n-HA1, CSi-Mg/n-HA3). After 14 days, cells were fixed with 4 % (v/v) paraformaldehyde and stained with alizarin red S (Servicebio) (2 %) at pH 4.2 for 20 min and then washed with deionized water. The samples were air-dried, and photos were taken under a light microscope.

*2.8. Statistical analysis*

All the data above were expressed as the mean value ± standard deviation (SD) and analyzed with the one-way analysis of variance (ANOVA). In all cases the results were considered statistically significant at a p-value < 0.05.

## 3. Results and discussion

*3.1. Primary characterization of the powders and scaffolds*

Fig. 1 shows the brief illustration of the study. The architecture of the scaffolds was fabricated by the 3D printing technique and nano-HA surface layer was obtained via immersion method. The liquid bridge in *n*-HA/ethanol makes *n*-HA particles adhere to the surface of the support [33]. After the support is removed and dried, solid bridge is formed between particles and particles as well as between particles and the support, making *n*-HA particles adsorb on the surface of the support [34,35]. SA solution not only protects the *n*-HA adsorbed on the surface of the scaffold, but also serves as the base surface for the next layer of *n*-HA adsorbed. Finally, the composite scaffolds were fabricated with interconnected porous CSi-Mg scaffolds as the architecture and *n*-HA as the surface.

XRD pattern of the *n*-HA particles confirmed that *n*-HA exhibited a typical phase composition of HA (PDF#09–0432). The spectral data confirmed that the CSi-Mg sample has high crystallinity, which coincides with the wollastonite-2 M (β-CSi; PDF# 27–0088), indicating pure wollastonite nature (Fig. 2A). According to the SEM observation, the particle size of CSi-Mg powders after calcination are all<10 μm (Fig. 2B) and the particle size of *n*-HA powders are<100 nm (Fig. 2C). Also, it is worth noting that the measured Mg content in CSi-Mg powder was 2.10 wt%, which was close to the theoretical data (2.12 wt%) calculated by the 10 % Ca substitution by Mg in the stoichiometric wollastonite.

The fracture surface of the scaffolds without and with *n*-HA are shown in Fig. 2D and 2E. The horizontal side pores with rectangular morphology could be observed and the surface of the scaffold is covered with *n*-HA layer. Fig. 2F and 2G show the influence of different immersion time (5 min-15 min) in *n*-HA/ethanol solution and different SA concentration (1.0 %-2.0 %) on the thickness of *n*-HA layer. The thickness of *n*-HA layer gradually increases with increasing soaking time. However, the thickness increases slowly with the increase of immersion time from 10 min to 15 min. When immersion in 1.5 % SA solution, the composite scaffolds showed thicker *n*-HA layer (~16 μm) than those immersion in a lower (1.0 %) or higher (2.0 %) concentration. This is because the flow performance of 1.0 % SA solution is too good to take away the *n*-HA of the scaffold surface. When the concentration exceeds 2.0 %, the SA solution will be difficult to enter the pores of the scaffolds. Finally, we choose immersion time for 10 min, SA concentration for 1.5 % to continue next experiment.

The thickness of *n*-HA layers with varying *n*-HA/ethanol solution concentration (0.1 g/ml-0.2 g/ml) and coating number (1–3) is shown Fig. 2H and 2I. The thickness of the *n*-HA layer increased with increasing *n*-HA/ethanol solution concentration and it also increased with increasing coating number. When solution concentration at 0.2 g/ml, the *n*-HA layer of CSi-Mg/n-HA1 was evenly distributed on the surface of the CSi-Mg scaffold. With the increase of coating number from 1 to 3, the thickness of the *n*-HA layers was not uniform. Even when the coating number exceeds 3 times, the pore of scaffold will be blocked. Both the CSi-Mg/*n*-HAx (x = 1, 2, 3) composite scaffolds with solution concentration at 0.1 g/ml and 0.15 g/ml had uniform surface *n*-HA layers, and the CSi-Mg/*n*-HA composite scaffold with solution concentration at 0.15 g/ml had suitable *n*-HA layer thickness. These investigations suggest that the solution concentration and coating number are important factors to influence *n*-HA layer thickness of the composite scaffold. Finally, we choose *n*-HA/ethanol solution (0.15 g/ml) and CSi-Mg/n-HA1 (5 μm) and CSi-Mg/n-HA3 (15 μm) to continue next experiment.

*3.2. Degradation behavior of the scaffolds in vitro*

To further understand the effect of surface coating on mechanical strength attenuation of the scaffolds, especially the effect of coating thickness on strength, the CSi-Mg/*n*-HAx scaffolds were kept in SBF up to 3 weeks (Fig. 3A). Fig. 3B shows the change of pH value in SBF with the increase of soaking time. It is seen that the pH value in SBF gradually increased when immersing the CSi-Mg scaffolds, which may be related to the binding effect between $SiO_3^{4-}$ released during the degradation of scaffolds and $H^+$ in solution [11]. In the solution of CSi-Mg/n-HA1 and CSi-Mg/n-HA3, the pH value decreased and then increased. Scaffolds surface with adsorption by sodium alginate, dissolved in solution, $Ca^{2+}$ in solution combined with sodium alginate formation water gel [36]. $H^+$ as cationic complement the loss of $Ca^{2+}$ in the solution, cause a drop in pH value. The pH value of the CSi-Mg/n-HA3 solu-

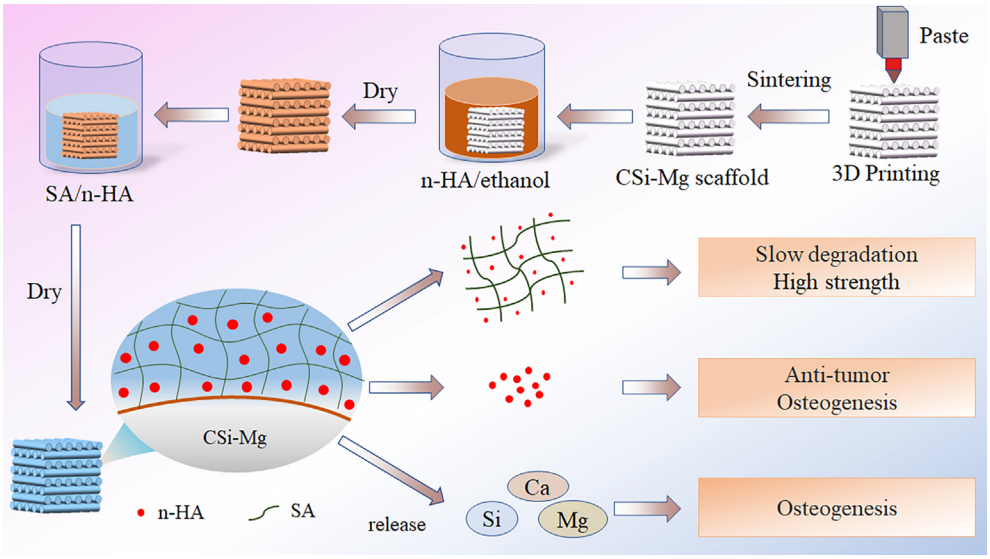


**Fig. 1.** The brief illustration of the study.

tion is higher because the CSi-Mg/n-HA3 scaffold has more *n*-HA particles. High *n*-HA proportion exhibit high concentration of hydroxide (OH) ion cause a rise in pH value [37]. The pH value of the solution gradually increased under the influence of the degradation of the scaffold and *n*-HA. It could be seen that the solution was flat and weak alkaline at 21 days, which is favorable for osteogenic cell growth in the porous scaffolds.

Fig. 3C shows the change in weight as a function of immersion time. The weight of all CSi-Mg/*n*-HAx scaffolds reduced within the initial 1 week, but the pure CSi-Mg scaffolds had the highest weight loss rate (Fig. 3D). From the weight change of the scaffolds in Fig. 3C, the weight loss of the CSi-Mg/*n*-HAx (x = 1, 3) scaffolds is mainly caused by the *n*-HA falling from the scaffolds surface. This shows that the *n*-HA layer can stop the CSi-Mg scaffolds from degrading. The *n*-HA particles on the surface of the CSi-Mg/n-HA1 scaffold is less than that of CSi-Mg/n-HA3, so its weight loss rate is lower due to the stronger coating effect. After soaking for 2 weeks, the weight loss of the CSi-Mg/n-HA3 scaffolds was the largest, which was due to the *n*-HA dropped or degraded on the surface of the scaffolds. The *n*-HA layer dropped and degradation on the CSi-Mg/n-HA1 scaffold in the second week were also the main factors of the weight loss. The weight loss rate of all CSi-Mg/*n*-HAx scaffolds tended to be gentle after 3 weeks. Although the weight loss rate of the CSi-Mg/n-HA3 scaffold was 7.3 % after 3 weeks, its weight value was still bigger than the other two scaffolds.

As for the strength decay during this process, the compressive strength of CSi-Mg scaffolds decreased by nearly 20 % within 3 weeks, from ~ 91 MPa to ~ 73 MPa. The CSi-Mg/*n*-HAx (x = 1, 3) scaffolds changed slowly with appreciable compressive strength (81–91 MPa) after the whole immersion stage of 3 weeks (Fig. 3E). Overall, all the composite scaffolds showed the same trend that compressive strength decreased continuously as a function of time. The CSi-Mg/n-HA3 scaffolds showed the largest compressive strength (91 MPa) in 3 weeks. The change trend of elastic modulus is consistent with that of compressive strength (Fig. 3F). The *n*-HA layer reduced the porosity of the scaffolds and improved mechanical properties correspondingly. This can also be confirmed by the representative stress–strain curves for the samples during compression test (Fig. 3G). In addition, the SA in the *n*-HA layer dissolved in solution to form hydrogels, which will fill tiny gaps on the surface of the scaffold to improve its mechanical properties. It implies that the surface adsorption of *n*-HA and SA contributed to the higher mechanical endurance of the scaffolds. It is reasonable to conclude that, the CSi-Mg/*n*-HAx composite scaffolds show a good mechanical stability in aqueous medium with physiological pH condition, which would be adapt for the large segmental bone defect applications.

### 3.3. Surface reactivity of scaffolds

To further determine the suitability of the CSi-Mg/*n*-HAx scaffolds for application in bone repair, their surface reactivity was tested by immersing SBF for 0–3 weeks (Fig. 4). The spherical particles are deposited on the surface of the CSi-Mg scaffold within 1 week. After 3 weeks, the surface of the scaffolds was covered with a layer of HA mineral. The formation of biomimetic HA is responsible for the strong bonding between implants and host bone tissue. However, there was no HA mineral on the surface of the CSi-Mg/n-HA1 scaffold until the third week, probably because the SA on the surface of the scaffold formed hydrogel with $Ca^{2+}$ in the solution [36]. The reduction of $Ca^{2+}$ affects the formation of HA mineral. There was also no HA mineral on the surface of the CSi-Mg/n-HA3 scaffolds within 3 weeks and the CSi-Mg/n-HA3 scaffold needed more time to form the mineral layer.

### 3.4. anti-tumor effect in vitro

SEM was used to observe the morphology and attachment of human osteosarcoma MG63 cells cultured on three kinds of scaffolds for three days. We found that cells spread well on the CSi-Mg scaffolds (Fig. 5A) and had good cellular state (Fig. 5D). It was seen that MG63 cells did not well attach on the surface of the CSi-Mg/n-HA1 scaffolds (Fig. 5B). On the contrary, the cells slightly curled (Fig. 5E) and did not spread well. In addition, the MG63 cells did not attach well on the surface of the CSi-Mg/n-HA3 scaffolds (Fig. 5F) and spread further reduce (Fig. 5C). These results shows that the *n*-HA layer could inhibit the growth of human bone MG63 tumor cells [38–40].

The apoptotic rates of the MG63 cells treated with different scaffolds extract for 7 days were quantified (Fig. 6A, B). CSi-Mg/*n*-HA scaffolds increased the apoptotic rate of the cells in a dose-dependent manner. With the coating time rising from 1 to 3, the percentage of early and late apoptotic cells increased from 4.46, 12.98 % to 6.45, 29.15 %. This suggests that the coating on the scaf-

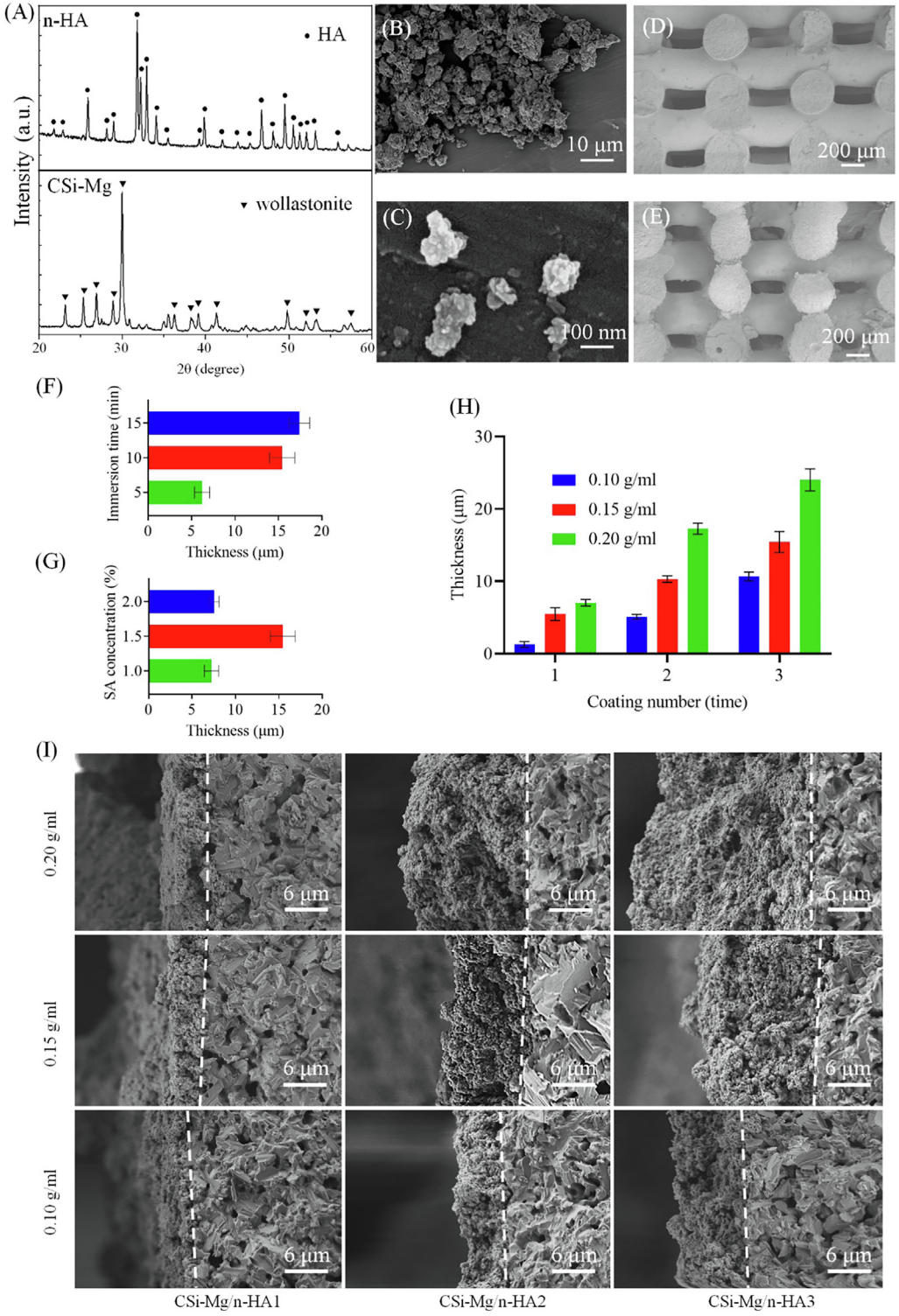


**Fig. 2.** Characterization of powders and scaffolds. (A) XRD patterns of *n*-HA and CSi-Mg powders. (B) SEM image of CSi-Mg powders. (C) SEM image of *n*-HA powders. (D) SEM micrographs of fracture surface of CSi-Mg scaffold and (E) CSi-Mg/*n*-HA scaffold. (F) Thickness of *n*-HA layer after soaking for 5 min, 10 min and 15 min. (G) Thickness of *n*-HA layer after soaking at 1.0 %, 1.5 % and 2.0 % SA solution. (H) Thickness of *n*-HA layer in different concentrations of *n*-HA/ethanol solution and different coating times. (I) SEM micrographs of CSi-Mg/*n*-HA composite scaffolds using different concentrations of *n*-HA/ethanol solution and different coating times. *n*-HA layer is represented on the left side of the dot line.

folds can effectively promote cell apoptosis [41]. The scanning microscopy images in Fig. 6C indicated different cells in cell viability staining experiment (red fluorescence was used to dye the died cells, green fluorescence was used to dye live cells). In CSi-Mg/n-HA1 and CSi-Mg/n-HA3 groups, strong red fluorescence of 7 days indicates a high number of death cells. The survival rate (Fig. 6D) indicates that CSi-Mg/n-HA1 and CSi-Mg/n-HA3 scaffolds are able to promote cell death. By day 7, CSi-Mg/n-HA3 scaffold induced about 50 % of cell death for human osteosarcoma cells (MG-63) in vitro. In the cell morphology staining diagram (Fig. 6E), blue flu-

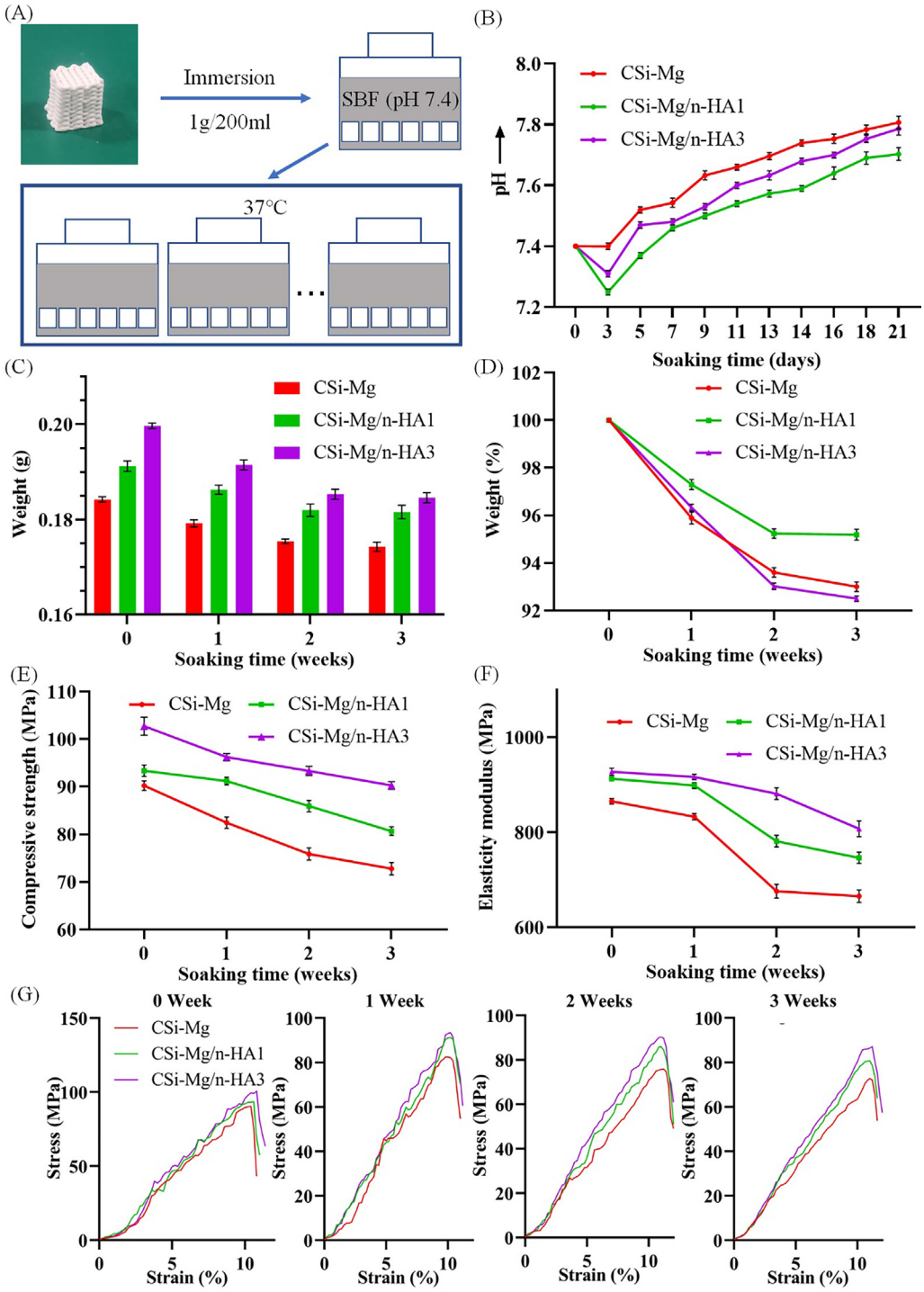


**Fig. 3.** Degradation test in SBF (pH 7.4) for 3 weeks. (A) Schematic illustration of the scaffolds soaking in SBF. (B) pH changes in SBF. (C) Changes in weight of the scaffolds as a function of soaking time. (D) Changes in weight (%) of the scaffolds as a function of soaking time. (E) Compressive strengths and (F) the elastic modulus of the scaffolds as a function of time. The elastic modulus in (F) was calculated from the slope of the linear segment of (G) the stress strain curve.

orescence was used to dye the DAPI and green fluorescence was used to dye ACTIN. The fluorescence intensity shows CSi-Mg group exists more cells. This indicates that CSi-Mg/n-HA1 and CSi-Mg/n-HA3 scaffolds are able to inhibit cell proliferation. In Fig. 6F, we performed a colony formation assay using the extracts of scaffolds (the cells in the plate were stained blue), and compared with the control group, fewer clones were formed in the CSi-Mg/n-HA1 and CSi-Mg/n-HA3 groups. Number of clone formation shows it clearly (Fig. 6G). On the other hand, CCK-8 assay (Fig. 6H) also showed that CSi-Mg/*n*-HAx (x = 1, 3) scaffolds could inhibit the proliferation of tumor cells.

Transwell migration assay (Fig. 7A) showed that the minimum number of tumor cells migrated through the chamber after treatment with the CSi-Mg/n-HA1 scaffolds extract and the CSi-Mg/n-HA3 scaffolds extract (Fig. 7B). Wound-healing assay (Fig. 7C) showed tumor cells co-cultured with the CSi-Mg/n-HA3 scaffolds extract (Fig. 7C c5, c6) significantly delayed wound closure compared to the CSi-Mg scaffolds extract medium (Fig. 7C c1, c2) or

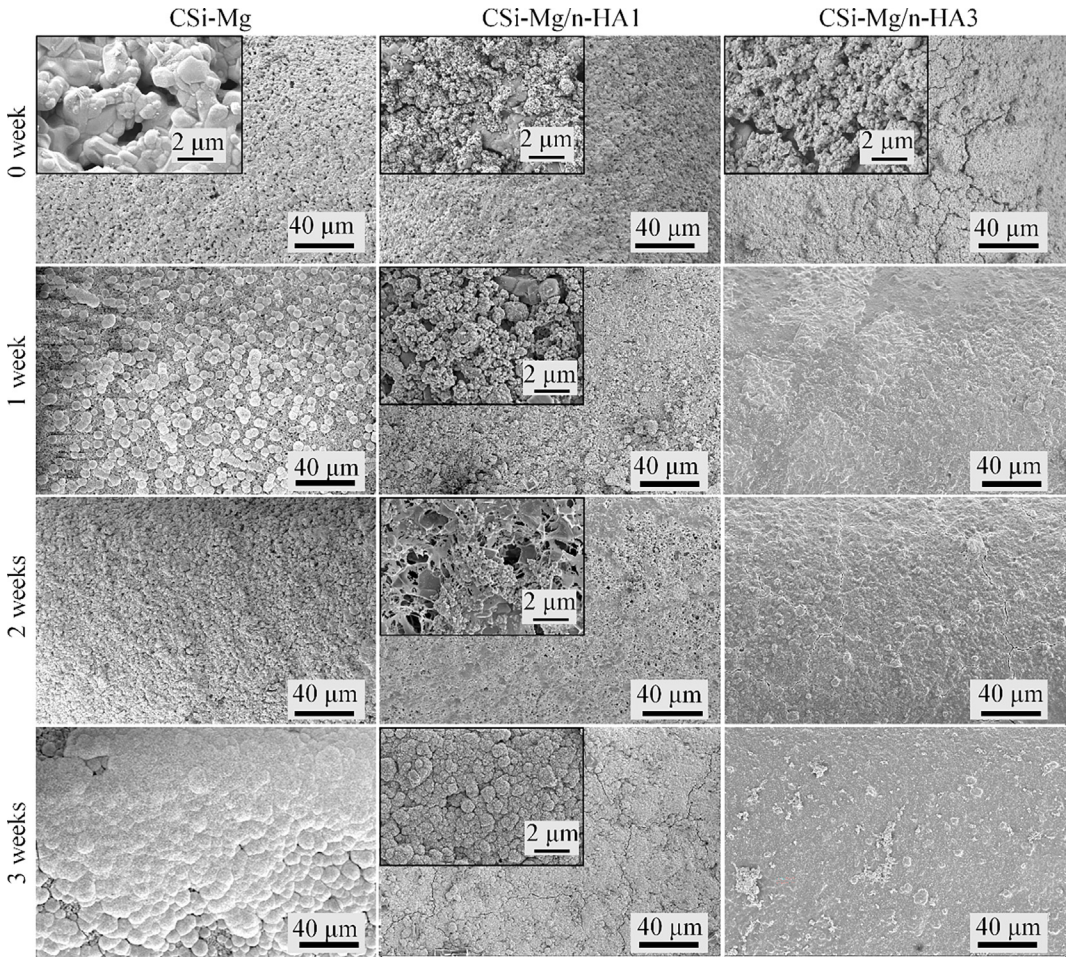


**Fig. 4.** SEM images of the surface of scaffolds after soaking in SBF for 1–3 weeks.

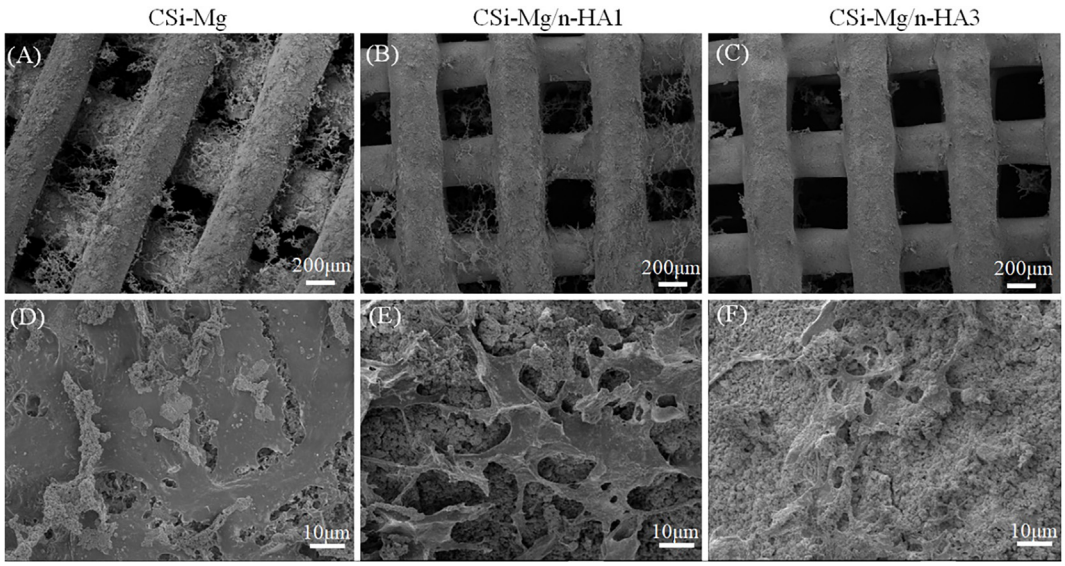


**Fig. 5.** SEM images of MG63 cultured in three kinds of scaffolds for three days. (A, D) CSi-Mg scaffolds. (B, E) CSi-Mg/n-HA1 scaffolds. (C, F) CSi-Mg/n-HA3 scaffolds.

CSi-Mg/n-HA1 (Fig. 7C c3, c4) scaffolds extract medium. The area of wound healing (Fig. 7D) suggested that the coated scaffolds can decrease the migration of tumor cells [42]. In RNA extraction and qRT-PCR, our results demonstrated that gene expression of Ki-67 (Fig. 7E) decreased indicating a less cell proliferative activity and more induced apoptosis [43]. It was found that Bcl-2 gene was inhibited in the experimental group compared with the control group (Fig. 7E), The expression of Bcl-2 gene can inhibit cell apop-

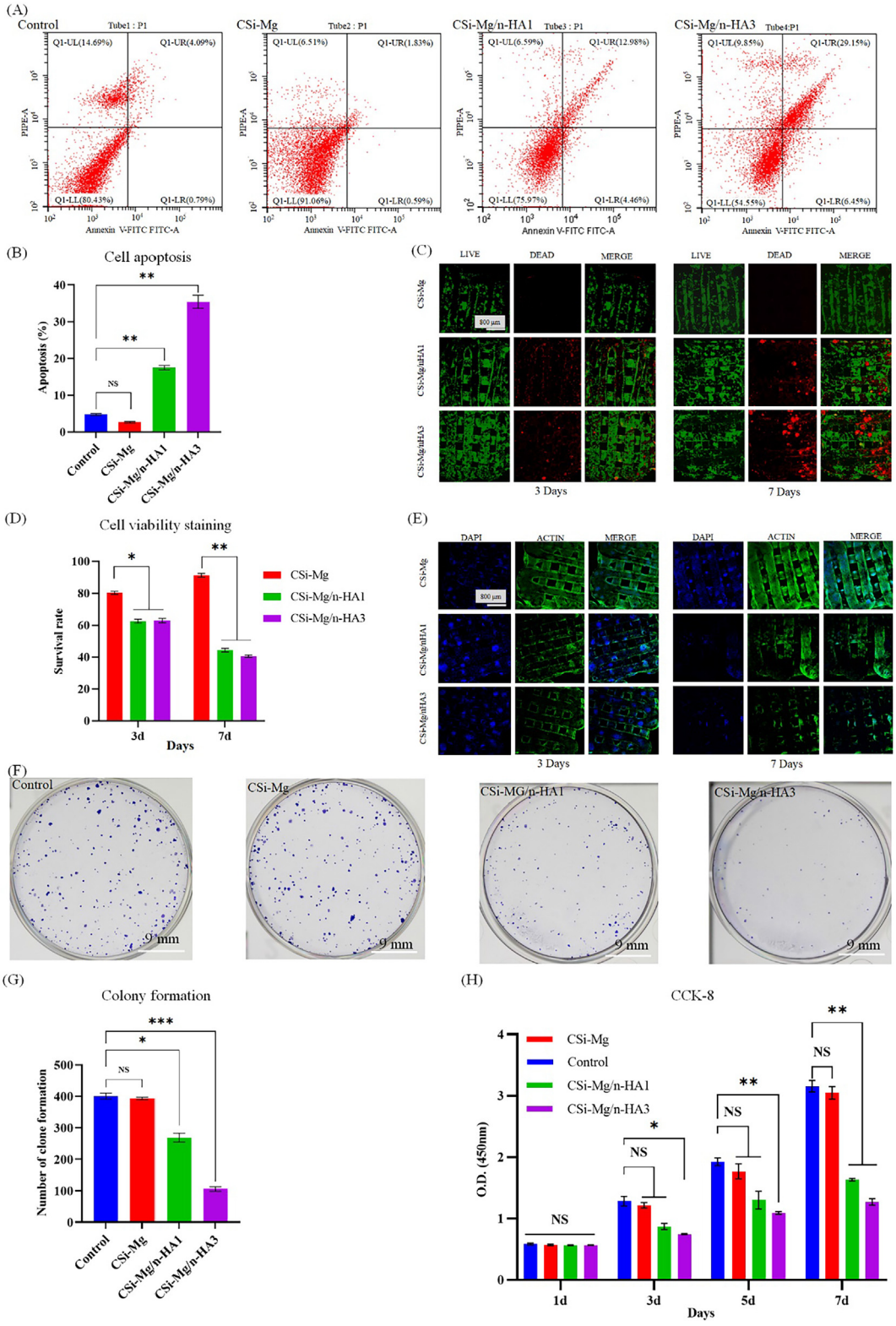


**Fig. 6.** Scaffolds can inhibit the proliferation of tumor cells in vitro. (A) Representative point plot of apoptosis detection results of MG63 human osteoma cells treated with different scaffold extracts for 7 days and (B) apoptosis rates of each group. (C) Tumor cell viability staining and (D) the survival rate. (E) Cell morphology staining. (F) Colony formation and (G) number of clone formation. (H) CCK-8 assay. (*p < 0.05, **p < 0.01, ***p < 0.001) (n = 6).

tosis [44]. The expression of Bcl-2 gene in the experimental group was decreased, indicating that the experimental group promoted cell apoptosis. The activity of caspase-3 was detected by spectrophotometry (Fig. 7F), and the CSi-Mg/n-HA1 and CSi-Mg/n-HA3 groups were significantly higher than the control group. This indicates that the activation of caspase-3 promoted cell apoptosis [32].

The mechanism of *n*-HA induced tumor cells apoptosis has been extensively investigated but is still debating, studies have shown that particles<5 μm could induce more obvious cytotoxicity [26–

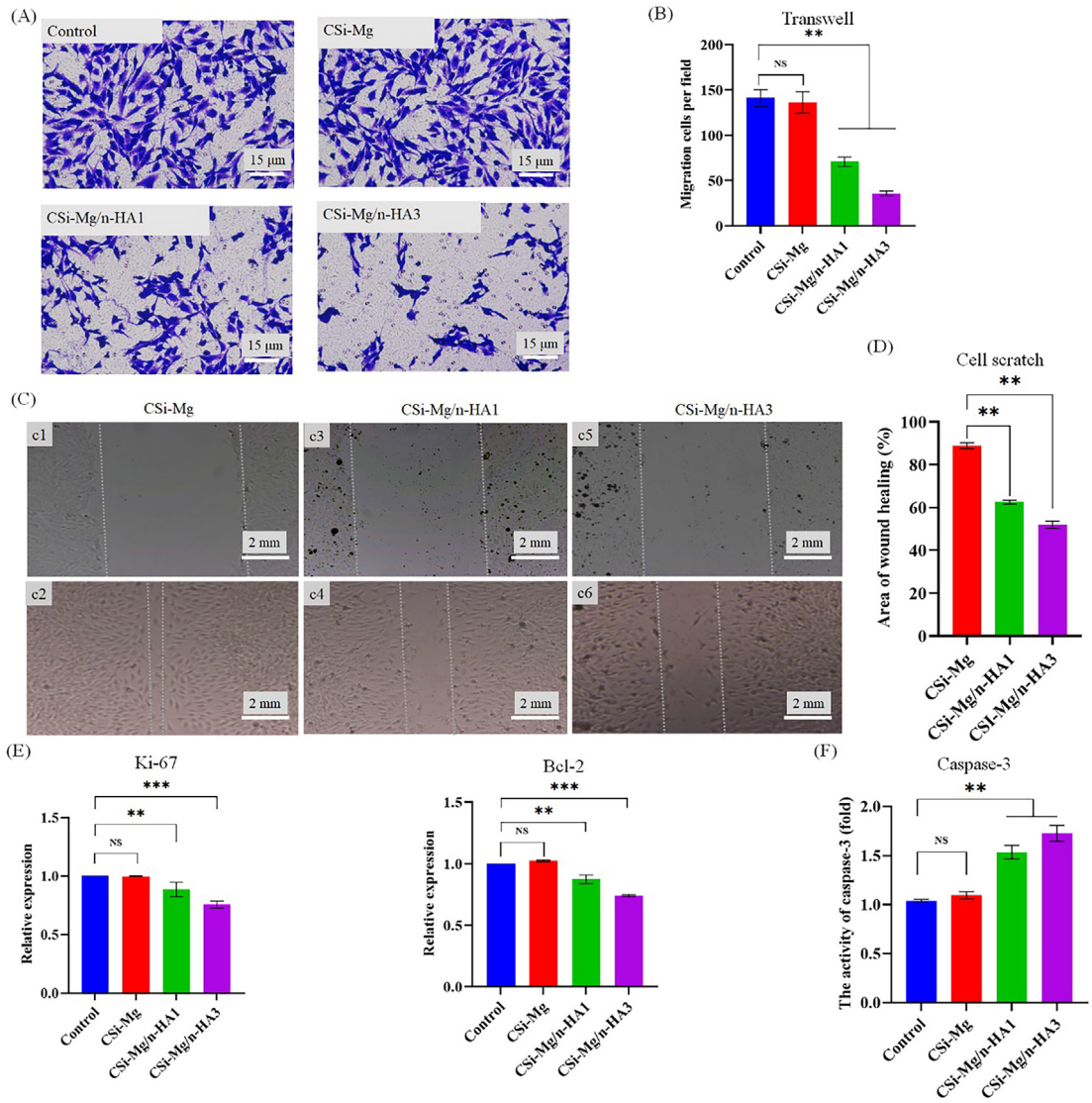


**Fig. 7.** Scaffolds can reduce cell migration in vitro. (A) Transwell experiment and (B) migration cells per field. (C) Cell scratch assay and (D) area of wound healing (%). (E) RNA extraction and qRT-PCR. (F) Caspase-3 activation test. (*p < 0.05, **p < 0.01, ***p < 0.001) (n = 6).

28]. Probably, *n*-HA particles were swallowed by the tumor cell and stimulate cells in the cytoplasm, cause MG63 cells death [45]. After endocytosis, *n*-HA would bind to ribosome and accumulate around the endoplasmic reticulum, resulting in arresting cell cycle and inhibiting protein synthesis in tumor cells, then *n*-HA could induce activated mitochondrial-dependent apoptosis in tumor cells [46]. The expression of caspase-3 gene is the most important component of apoptosis, and it is the activation of caspase-3 gene that initiates apoptosis. Caspase-3 protein function as effector to cleave various substrates including cytokeratins, the plasma membrane cytoskeletal protein alpha fodrin, the nuclear protein and others, that ultimately cause the morphological and biochemical changes seen in apoptotic cells. Caspase-3 gene can also induce cytoskeletal recombination and cell disintegration into apoptotic bodies. Therefore, *n*-HA leads to more apoptosis of MG63 cells through higher expression of caspase-3 gene [32]. Ki-67, a gene that may be a marker of proliferating cells, involved in chromatin compaction. Its expression is altered in many tumor types including osteosarcomas. Bcl-2 gene encodes an integral outer mitochondrial membrane protein that blocks the apoptotic death of some cells. In our experiment, *n*-HA could inhibit the expression of Ki-67 gene and Bcl-2 gene, results in decreased protein synthesis of Ki-67 and Bcl-2 protein [43,44], which could promote MG63 cells apoptosis. Transwell assay and cell scratch experiment in this paper showed that CSi-Mg/*n*-HA scaffold could significantly delay cell invasion and migration, which may be related to the combination of low expression of Ki-67 and Bcl-2 protein and high expression of caspase-3 protein reduces the ability of cells to migration and invasion of tumor cells. In this paper, CSi-Mg/n-HA3 scaffold has a better effect on promoting tumor cell apoptosis and reducing migration than other scaffolds, which is related to the amount of *n*-HA on the surface of the scaffold. More *n*-HA on the surface of CSi-Mg/n-HA3 scaffold enhances its anti-tumor effect significantly. In this work, CCK-8 assay, apoptosis assay, viability staining, morphological staining and cell cloning experiments all proved that the scaffold could inhibit the proliferation of MG63. Through cell scratch experiment and transwell assay, it was verified that the scaffold could inhibit the migration of tumor cells.

### 3.5. In vitro osteogenesis

In order to study the osteogenic properties of scaffolds, we conducted some experiments with Rat BMSC. In cell viability staining, the scanning microscopy images in Fig. 8A indicated different cells

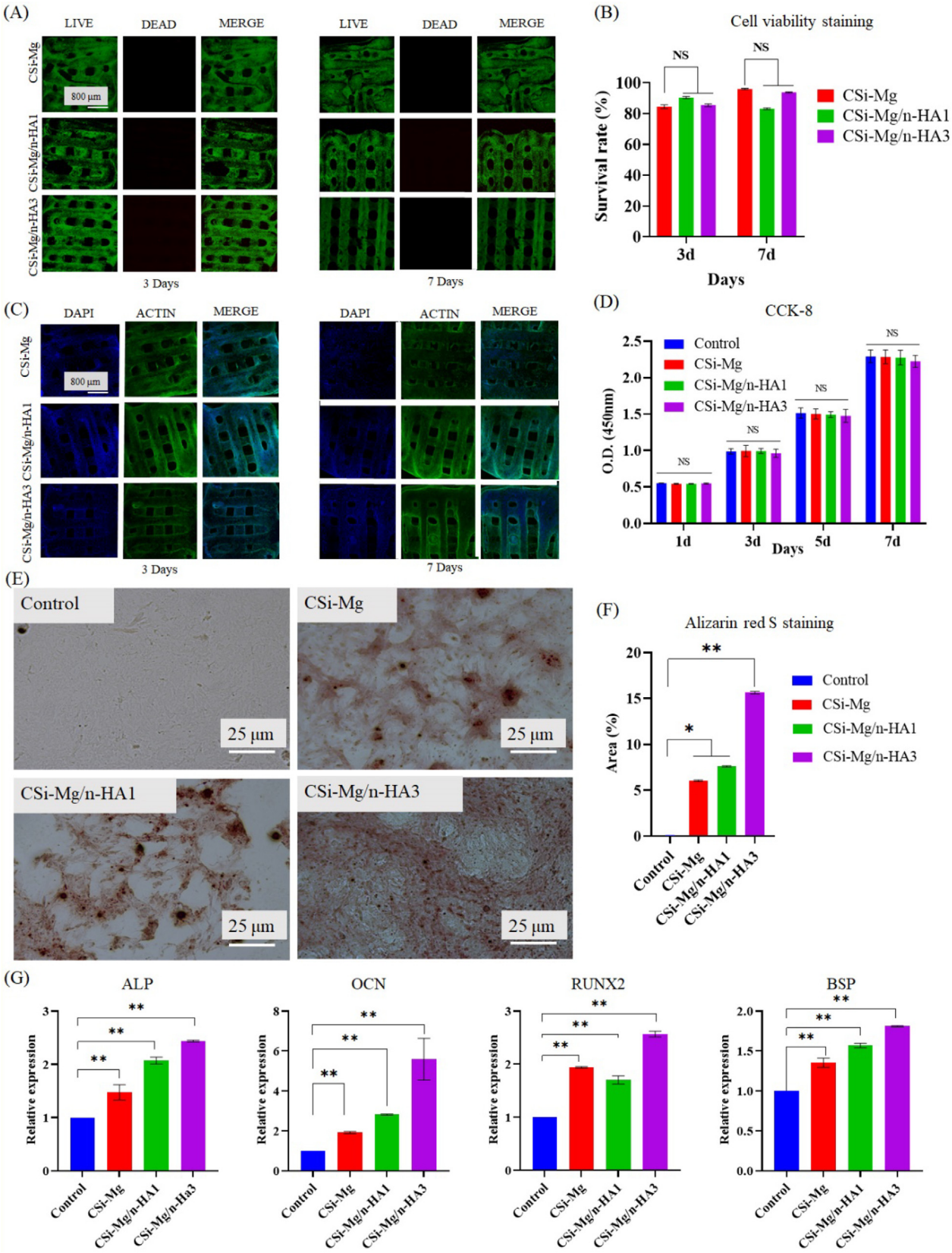


**Fig. 8.** Scaffolds can promote osteogenic of Rat BMSC in vitro. (A) Cell viability staining and (B) survival rate. (C) Cell morphology staining. (D) CCK-8 assay. (E) Alizarin red S staining and (F) dyeing area (%). (G) RNA extraction and QRT-PCR. (*p < 0.05, **p < 0.01, ***p < 0.001) (n = 6). (For interpretation of the references to colour in this figure legend, the reader is referred to the web version of this article.)

(red fluorescence was used to dye the died cells, green fluorescence was used to dye live cells). We could see that each group of scaffolds had the similar fluorescence. There are no obvious dead cells in each group and survival rate showed that each group of scaffolds expressed a good survival rate on Rat BMSC (Fig. 8B) [47]. This indicated that all scaffolds have good biocompatibility. In the cell morphology staining diagram (Fig. 8C), blue fluorescence was used to dye the DAPI and green fluorescence was used to dye ACTIN. The fluorescence intensity, indicates they had no significant effect on the growth of Rat BMSC, this indicated that the cells can live on the scaffolds. On the other hand, CCK-8 experiment (Fig. 8D) showed that each group of scaffolds did not affect the proliferation of Rat BMSC. The difference was not statistically significant compared to the control group. Then, alizarin-red S assay was done to study calcium deposition. In the Alizarin-red S staining experiment (Fig. 8E) and dyeing area (Fig. 8F), it could be seen that the CSi-Mg/n-HA3 scaffolds had better osteogenic effect [48]. In RNA extraction and qRT-PCR experiments (Fig. 8G), the activities of ALP, BSP, OCN and RUNX2 were gradually improved with the increase of coating times, indicating that the more adsorption times, the better osteogenic performance [49]. This proves that CSi-Mg/*n*-HAx scaffolds have better osteogenic effect from the genetic level.

We use Rat BMSC to explore the effect of surface coating on the osteogenic performance of the scaffold. HA is investigated extensively due to its excellent bioactivity, biocompatibility, osteoconductivity, and chemical stability. It exhibits the same structure, function and chemical composition as bone. CSi-Mg scaffold can release of calcium, silicon and magnesium ions during the degradation process, which is good for osteogenesis. There were more calcium deposits on the surface of CSi-Mg/n-HA3 scaffold in this paper, indicating that the scaffold had good osteogenic properties [50]. In addition, we also found that CSi-Mg/*n*-HAx (x = 1,3) scaffolds could induce relatively high expression of ALP, OCN, BSP and RUNX2 gene. CSi-Mg/n-HA3 scaffold has a higher expression than other scaffolds, which is related to the amount of *n*-HA on the surface of the scaffold. More *n*-HA on the surface of CSi-Mg/n-HA3 scaffold enhances its osteogenic effect significantly. The *n*-HA particle on the surface of scaffold can enter Rat BMSC by endocytosis. By lysosomes, they are decomposed into calcium and phosphate ions [51]. Calcium ions are able to activate the sAC, cAMP, Epac, and Rap1 proteins. Followed by starting Rap1 activation, other proteins in the cell, such as Raf1 and PI3K, are activated [52]. PI3K-AKT is an essential pathway in proliferation, differentiation and cell survival, for the activation of AKT protein [53]. Upon activation of AKT, the CREB protein is phosphorylated and subsequently enters the cell nucleus and acts as a transcription factor which can provides transcription for ALP, OCN, BSP and RUNX2 genes [54]. By regulating levels of diphosphate (PPi), alkaline phosphatase (ALP) gene plays a key role in skeletal mineralization. Osteocalcin (OCN) gene expression produces OCN protein, which constitutes 1–2 % of the total bone protein. It binds strongly with apatite and calcium. Bone sialoprotein (BSP) gene expression produces BSP, BSP binds tightly to hydroxyapatite, probably BSP is important to cell-matrix interaction. Transcription factor of RUNX2 gene involved in osteoblastic differentiation and skeletal morphogenesis, it is essential for the maturation of osteoblasts and both intramembranous and endochondral ossification. ALP, OCN, BSP, and RUNX2 are some of the most important genes expressed by osteoblasts, and they collectively contribute to the formation of the osseous matrix and controlled calcification. Different bone matrix proteins have different biological functions in bone formation, scaffolds enhance the expression of these genes and thus promote osteogenic properties[55]. The expression of these genes leads the cell to differentiate osteogenesis. In general, scaffolds with *n*-HA adsorbed on the surface have good osteogenic properties.

## 4. Conclusions

In summary, this study developed a novel bioactive scaffold, the composite bioceramic scaffold was fabricated with interconnected porous magnesium-doped wollastonite (CSi-Mg) scaffolds as the architecture and nano-hydroxyapatite (*n*-HA) as the surface. Nano-hydroxyapatite coating can effectively slow down the degradation of CSi-Mg scaffolds. SBF immersion experiment in vitro showed that the composite scaffolds had good mechanical retention and the CSi-Mg/n-HA3 scaffold still had a high compressive strength (over 90 MPa) after three weeks. CSi-Mg/n-HA3 scaffold induced about 50 % of cell death for human osteosarcoma cells (MG-63) in vitro, indicating that the composite scaffolds had good anti-tumor effect. In addition, we used Rat BMSC to study the effect of the scaffolds on the osteogenic properties, and the results showed that the scaffolds with surface modification have a good effect on the osteogenic properties of the scaffold. We believe this approach presents a promising strategy for developing high strength and anti-tumor bioceramic scaffolds, indicating a promising clinical tool for the treatment of tissue damage after resection of osteosarcoma.

## CRediT authorship contribution statement

**Huifeng Shao:** Writing – original draft, Funding acquisition, Resources, Conceptualization, Validation, Supervision. **Zhuoluo Jing:** Writing – original draft, Resources, Validation. **Pengcheng Xia:** Writing – original draft, Resources, Validation. **Tao Zhang:** Resources. **Zhiheng Nian:** Resources. **Wanshun Liu:** Resources. **Jiahua Zhu:** Resources. **Youping Gong:** Resources. **Rougang Zhou:** Resources. **Yong He:** Writing – review & editing, Validation. **Qingqiang Yao:** Funding acquisition, Writing – review & editing, Validation.

## Data availability

Data will be made available upon reasonable request to the corresponding author.

## Declaration of Competing Interest

The authors declare that they have no known competing financial interests or personal relationships that could have appeared to influence the work reported in this paper.

## Acknowledgments

This work was supported by the National Natural Science Foundation of China (51805475, 82072400), Zhejiang Provincial Natural Science Foundation of China (LY22E050011), Zhejiang Provincial Postdoctoral Research Funds (ZJ2022009), Postdoctoral Science Foundation of China (2022M722736), Fundamental Research Funds for the Provincial Universities of Zhejiang (GK229909299001-304), Open Foundation of the State Key Laboratory of Fluid Power and Mechatronic Systems (GZKF-202102), Jiangsu Key Laboratory of 3D Printing Equipment and Manufacturing (3DL202105), the Natural Science Foundation of Jiangsu Province (BK20200001) and the Opening Project of State Key Laboratory of High Performance Ceramics and Superfine Microstructures (SKL202010SIC).

## Appendix A. Supplementary material

Supplementary data to this article can be found online at https://doi.org/10.1016/j.matdes.2022.111464.

## References


[1] J. Liao, R. Han, Y. Wu, Z. Qian, Review of a new bone tumor therapy strategy based on bifunctional biomaterials, Bone Res 9 (2021) 18.

[2] D. Chen, Z. Zhao, Z. Huang, D.C. Chen, X.X. Zhu, Y.Z. Wang, Y.W. Yan, S. Tang, S. Madhavan, W. Ni, Z.P. Huang, W. Li, W. Ji, H. Shen, S. Lin, Y.Z. Jiang, Super enhancer inhibitors suppress MYC driven transcriptional amplification and tumor progression in osteosarcoma, Bone Res 6 (2018) 11.

[3] W. Dang, Y. Jin, K. Yi, E. Ju, C. Zhuo, H. Wei, X. Wen, Y. Wang, M. Li, Y. Tao, Hemin particles-functionalized 3D printed scaffolds for combined photothermal and chemotherapy of osteosarcoma, Chem. Eng. J. 422 (2021) 129919.

[4] S. Pan, J. Yin, L. Yu, C. Zhang, Y. Zhu, Y. Gao, Y. Chen, 2D MXene-integrated 3D-printing scaffolds for augmented osteosarcoma phototherapy and accelerated tissue reconstruction, Adv. Sci. 7 (2020) 1901511.

[5] K. Li, K. Cai, Q. Ran, D. Jiang, Biomimetic triphase composite scaffolds with antibacterial and anti-tumor potentials for bone repair, Mater. Lett. 256 (2019) 126590.

[6] H. Belaid, S. Nagarajan, C. Teyssier, C. Barou, J. Bares, S. Balme, H. Garay, V. Huon, D. Cornu, V. Cavailles, M. Bechelany, Development of new biocompatible 3D printed graphene oxide-based scaffolds, Mater. Sci. Eng. C. Mater. Biol. Appl. 110 (2020) 110595.

[7] A. Suleman, P.P.D. Kondiah, M. Mabrouk, Y.E. Choonara, The Application of 3D-Printing and Nanotechnology for the Targeted Treatment of Osteosarcoma, Front. Mater. 8 (2021) 668834.

[8] C. Zhao, A. Shen, L. Zhang, K. Lin, X. Wang, Borocarbonitrides nanosheets engineered 3D-printed scaffolds for integrated strategy of osteosarcoma therapy and bone regeneration, Chem. Eng. J. 401 (2020) 125989.

[9] J. Xie, X. Yang, H. Shao, J. Ye, Y. He, J. Fu, C. Gao, Z. Gou, Simultaneous mechanical property and biodegradation improvement of wollastonite bioceramic through magnesium dilute doping, J. Mech. Behav. Biomed. 54 (2016) 60–71.

[10] J. Xie, H. Shao, D. He, X. Yang, C. Yao, J. Ye, Y. He, J. Fu, Z. Gou, Ultrahigh strength of three-dimensional printed diluted magnesium doping wollastonite porous scaffolds, Mrs. Commun. 5 (2015) 631–639.

[11] H. Shao, Y. He, J. Fu, D. He, X. Yang, J. Xie, C. Yao, J. Ye, S. Xu, Z. Gou, 3D printing magnesium-doped wollastonite/β-TCP bioceramics scaffolds with high strength and adjustable degradation, J. Eur. Ceram. Soc. 36 (2016) 1495–1503.

[12] Y. Yang, H. Wu, Q. Fu, X. Xie, Y. Song, M. Xu, J. Li, 3D-printed polycaprolactone-chitosan based drug delivery implants for personalized administration, Mater. Des. 214 (2022) 110394.

[13] Z. Li, H. Bai, Z. Wang, Y. Liu, M. Ren, X. Wang, W. Gao, Q. Li, M. Wu, H. Liu, J. Wang, Ultrasound-mediated rapamycin delivery for promoting osseointegration of 3D printed prosthetic interfaces via autophagy regulation in osteoporosis, Mater. Des. 216 (2022) 110586.

[14] Y. Gu, L. Wei, Z. Zhang, J. Van Dessel, R.B. Driesen, I. Lambrichts, R. Jacobs, L. Tian, Y. Sun, Y. Liu, C. Politis, BMP-2 incorporated biomimetic CaP coating functionalized 3D printed Ti6Al4V scaffold induces ectopic bone formation in a dog model, Mater. Des. 215 (2022) 110443.

[15] H. Ma, J. Luo, Z. Sun, L. Xia, M. Shi, M. Liu, J. Chang, C. Wu, 3D printing of biomaterials with mussel-inspired nanostructures for tumor therapy and tissue regeneration, Biomaterials 111 (2016) 138–148.

[16] H. Shao, M. Sun, F. Zhang, A. Liu, Y. He, J. Fu, X. Yang, H. Wang, Z. Gou, Custom repair of mandibular bone defects with 3D printed bioceramic scaffolds, J. Dent. Res. 97 (2018) 68–76.

[17] H. Shao, A. Liu, X. Ke, M. Sun, Y. He, X. Yang, J. Fu, L. Zhang, G. Yang, Y. Liu, 3D robocasting magnesium-doped wollastonite/TCP bioceramic scaffolds with improved bone regeneration capacity in critical sized calvarial defects, J. Mater. Chem. B. 5 (2017) 2941–2951.

[18] H. Shao, X. Ke, A. Liu, M. Sun, Y. He, X. Yang, J. Fu, Y. Liu, L. Zhang, G. Yang, Bone regeneration in 3D printing bioactive ceramic scaffolds with improved tissue/material interface pore architecture in thin-wall bone defect, Biofabrication 9 (2017) 025003.

[19] M. Sun, A. Liu, H. Shao, X. Yang, C. Ma, S. Yan, Y. Liu, Y. He, Z. Gou, Systematical evaluation of mechanically strong 3D printed diluted magnesium doping wollastonite scaffolds on osteogenic capacity in rabbit calvarial defects, Sci. Rep. 6 (2016) 1–14.

[20] C.K. Hagandora, M.A. Tudares, A.J. Almarza, The effect of magnesium ion concentration on the fibrocartilage regeneration potential of goat costal chondrocytes, Ann. Biomed. Eng. 40 (2012) 688–696.

[21] T. Ahmadi, A. Monshi, V. Mortazavi, M.H. Fathi, S. Sharifi, M. Kharaziha, L. Khazdooz, A. Zarei, M. Taghian Dehaghani, Fabrication and characterization of polycaprolactone fumarate/gelatin-based nanocomposite incorporated with silicon and magnesium co-doped fluorapatite nanoparticles using electrospinning method, Mater. Sci. Eng. C. Mater. Biol. Appl. 106 (2020) 110172.

[22] A. Bhattacharjee, S. Bose, 3D printed hydroxyapatite – Zn2+ functionalized starch composite bone grafts for orthopedic and dental applications, Mater. Des. 221 (2022) 110903.

[23] M. Stevanovic, D. Selakovic, M. Vasovic, B. Ljujic, S. Zivanovic, M. Papic, M. Zivanovic, N. Milivojevic, M. Mijovic, S.Z. Tabakovic, V. Jokanovic, A. Arnaut, P. Milanovic, N. Jovicic, G. Rosic, Comparison of Hydroxyapatite/Poly(lactide-co-glycolide) and Hydroxyapatite/Polyethyleneimine Composite Scaffolds in Bone Regeneration of Swine Mandibular Critical Size Defects, In Vivo Study, Molecules. 27 (2022) 1694.

[24] S. Biscaia, M.V. Branquinho, R.D. Alvites, R. Fonseca, A.C. Sousa, S.S. Pedrosa, A. R. Caseiro, F. Guedes, T. Patricio, T. Viana, A. Mateus, A.C. Mauricio, N. Alves, 3D Printed Poly(-caprolactone)/Hydroxyapatite Scaffolds for Bone Tissue Engineering: A Comparative Study on a Composite Preparation by Melt Blending or Solvent Casting Techniques and the Influence of Bioceramic Content on Scaffold Properties, Int. J. Mol. Sci. 23 (2022) 2318.

[25] H. Ma, C. Feng, J. Chang, C. Wu, 3D-printed bioceramic scaffolds: From bone tissue engineering to tumor therapy, Acta. Biomater. 79 (2018) 37–59.

[26] B. Li, B. Guo, H. Fan, X. Zhang, Preparation of nano-hydroxyapatite particles with different morphology and their response to highly malignant melanoma cells in vitro, Appl. Surf. Sci. 255 (2008) 357–360.

[27] S. Dey, M. Das, V.K. Balla, Effect of hydroxyapatite particle size, morphology and crystallinity on proliferation of colon cancer HCT116 cells, Mater. Sci. Eng. C. Mater. Biol. Appl. 39 (2014) 336–339.

[28] S.H. Chu, D.F. Feng, Y.B. Ma, Z.Q. Li, Hydroxyapatite nanoparticles inhibit the growth of human glioma cells in vitro and in vivo, Int. J. Nanomedicine. 7 (2012) 3659–3666.

[29] K. Zhang, Y. Zhou, C. Xiao, W. Zhao, H. Wu, J. Tang, Z. Li, S. Yu, X. Li, L. Min, Application of hydroxyapatite nanoparticles in tumor-associated bone segmental defect, Sci. Adv. 5 (2019) eaax6946.

[30] W. Liu, B. Wang, A. Duan, K. Shen, Q. Zhang, X. Tang, Y. Wei, J. Tang, S. Zhang, Exosomal transfer of miR-769-5p promotes osteosarcoma proliferation and metastasis by targeting DUSP16, Cancer Cell Int. 21 (2021) 1–17.

[31] M. Mazlam, N. Kamalaldin, Q. Ong, B. Yahya, A. Nurazreena, Effect of alginate on the properties of hydroxyapatite scaffold and cell migration assay study, Mater. Today: Proceedings. 17 (2019) 820–828.

[32] W. Li, F. Guo, X. Jiang, Y. Li, X. Li, Z. Yu, Compound ammonium glycyrrhizin protects hepatocytes from injury induced by lipopolysaccharide/florfenicol through oxidative stress and a MAPK pathway, Comp. Biochem. Physiol. C. Toxicol. Pharmacol. 225 (2019) 108585.

[33] S. Zhang, X. Li, Y. Du, A numerical model of discrete element – Liquid bridge – Liquid thin film system for wet deforming granular medium at low saturation, Powder. Technol. 399 (2022) 117217.

[34] L. Yang, M. Sega, J. Harting, Capillary-bridge forces between solid particles: Insights from lattice Boltzmann simulations, AIChE. J. 67 (2021) e17350.

[35] Y. Padmadisastra, R.A. Kennedy, P.J. Stewart, Solid bridge formation in sulphonamide-Emdex interactive systems, Int. J. Pharm. 112 (1994) 55–63.

[36] A. Sadeghianmaryan, S. Naghieh, Z. Yazdanpanah, H. Alizadeh Sardroud, N.K. Sharma, L.D. Wilson, X. Chen, Fabrication of chitosan/alginate/hydroxyapatite hybrid scaffolds using 3D printing and impregnating techniques for potential cartilage regeneration, Int. J. Biol. Macromol. 204 (2022) 62–75.

[37] B.C. You, C.E. Meng, N.F. Mohd Nasir, E.Z. Mohd Tarmizi, K.S. Fhan, E.S. Kheng, M.S. Abdul Majid, M.R. Mohd Jamir, Dielectric and biodegradation properties of biodegradable nano-hydroxyapatite/starch bone scaffold, J. Mater. Res. Technol. 18 (2022) 3215–3226.

[38] Y. Liu, T. Li, H. Ma, D. Zhai, C. Deng, J. Wang, S. Zhuo, J. Chang, C. Wu, 3D-printed scaffolds with bioactive elements-induced photothermal effect for bone tumor therapy, Acta. Biomater. 73 (2019) 531–546.

[39] W. Dang, B. Ma, Z. Huan, R. Lin, X. Wang, T. Li, J. Wu, N. Ma, H. Zhu, J. Chang, LaB6 surface chemistry-reinforced scaffolds for treating bone tumors and bone defects, Appl. Mater. Today. 16 (2019) 42–55.

[40] L. Chen, C. Deng, J. Li, Q. Yao, J. Chang, L. Wang, C. Wu, 3D printing of a lithium-calcium-silicate crystal bioscaffold with dual bioactivities for osteochondral interface reconstruction, Biomaterials 196 (2019) 138–150.

[41] Y. Li, Q. Leng, Y. Zhang, S. Lin, Q. Wen, Y. Lu, K. Xiong, H. Shi, Y. Liu, S. Xiao, L. Zhao, J. Wu, Z. Qian, S. Fu, Anaerobic bacteria mediated 'smart missile' targeting tumor hypoxic area enhances the therapeutic outcome of lung cancer, Chem. Eng. J. 438 (2022) 135566.

[42] W. Ma, H. Zhang, H. Ma, C. Wu, Iron manganese silicate incorporated bioactive hydrogels for therapy of skin tumor, Prog. Nat. Sci.- Mater. 32 (2022) 171–178.

[43] Z. Song, C. Li, D. Zhou, J. Liu, X. Qian, J. Zhang, Changes in Ki-67 in Residual Tumor and Outcome of Primary Inflammatory Breast Cancer Treated With Trimodality Therapy, Clin. Breast Cancer. (2022) e655–e663.

[44] Z. Zhang, L. Bai, L. Hou, H. Deng, S. Luan, D. Liu, M. Huang, L. Zhao, Trends in targeting Bcl-2 anti-apoptotic proteins for cancer treatment, Eur. J. Med. Chem. 232 (2022) 114184.

[45] F. Qing, Z. Wang, Y. Hong, M. Liu, B. Guo, H. Luo, X. Zhang, Selective effects of hydroxyapatite nanoparticles on osteosarcoma cells and osteoblasts, J. Mater. Sci. Mater. Med. 23 (2012) 2245–2251.

[46] Z. Chen, J. Deng, J. Cao, H. Wu, G. Feng, R. Zhang, B. Ran, K. Hu, H. Cao, X. Zhu, X. Zhang, Nano-hydroxyapatite-evoked immune response synchronized with controllable immune adjuvant release for strengthening melanoma-specific growth inhibition, Acta. Biomater. 145 (2022) 159–171.

[47] P. Lin, J. Shi, L. Ming, Y. Sheng, L. Song, M. Hong, Y. Zhang, An intelligent persistent luminescence nanoplatform with high-efficiency O2 utilization for continuous hypoxic tumors treatment, Chem. Eng. J. 442 (2022) 135638.

[48] M. Shokri, M. Kharaziha, H.A. Tafti, M.B. Eslaminejad, R.M. Aghdam, Synergic role of zinc and gallium doping in hydroxyapatite nanoparticles to improve osteogenesis and antibacterial activity, Mater. Sci. Eng. C. Mater. Biol. Appl. (2022) 112684.

[49] C. Deng, R. Lin, M. Zhang, C. Qin, Q. Yao, L. Wang, J. Chang, C. Wu, Micro/nanometer-structured scaffolds for regeneration of both cartilage and Subchondral bone, Adv. Funct Mater. 29 (2019) 1806068.

[50] Z. Chen, S. Han, M. Shi, G. Liu, Z. Chen, J. Chang, C. Wu, Y. Xiao, Immunomodulatory effects of mesoporous silica nanoparticles on

osteogenesis: From nanoimmunotoxicity to nanoimmunotherapy, Appl. Mater. Today. 10 (2018) 184–193.
[51] H. Maleki-Ghaleh, M. Hossein Siadati, A. Fallah, A. Zarrabi, F. Afghah, B. Koc, E. Dalir Abdolahinia, Y. Omidi, J. Barar, A. Akbari-Fakhrabadi, Y. Beygi-Khosrowshahi, K. Adibkia, Effect of zinc-doped hydroxyapatite/graphene nanocomposite on the physicochemical properties and osteogenesis differentiation of 3D-printed polycaprolactone scaffolds for bone tissue engineering, Chem. Eng. J. 426 (2021) 131321.
[52] Y.L. Zhang, R.C. Wang, K. Cheng, B.Z. Ring, L. Su, Roles of Rap1 signaling in tumor cell migration and invasion, Cancer, Biol. Med. 14 (2017) 90–99.
[53] M. Chen, Y. Cui, H. Li, J. Luan, X. Zhou, J. Han, Icariin Promotes the Osteogenic Action of BMP2 by Activating the cAMP Signaling Pathway, Molecules 24 (2019) 3875.
[54] H. Wang, J. Xu, P. Lazarovici, R. Quirion, W. Zheng, cAMP Response Element-Binding Protein (CREB): A Possible Signaling Molecule Link in the Pathophysiology of Schizophrenia, Front. Mol. Neurosci. 11 (2018) 255.
[55] Q. Zhang, L. Chen, B. Chen, C. Chen, J. Chang, Y. Xiao, C. Wu, F. Yan, Lithium-calcium-silicate bioceramics stimulating cementogenic/osteogenic differentiation of periodontal ligament cells and periodontal regeneration, Appl. Mater. Today. 16 (2019) 375–387.